Journal of composites science

MDPI

Article

Study of Nano-Mechanical, Electrochemical and Raman Spectroscopic Behavior of Al6061-SiC-Graphite Hybrid Surface Composite Fabricated through Friction Stir Processing

Abhishek Sharma, Vyas Mani Sharma, Baidehish Sahoo, Jomy Joseph and Jinu Paul *

Department of Mechanical Engineering, Indian Institute of Technology, Kharagpur 721302, India; abhi.sapne@gmail.com (A.S.); vyasmani@ymail.com (V.M.S.); baidehish.sahoo1367@gmail.com (B.S.); jomythoyalil@gmail.com (J.J.)

* Correspondence: jinu.paul@mech.iitkgp.ernet.in; Tel.: +91-322-228-2956

Received: 9 May 2018; Accepted: 24 May 2018; Published: 26 May 2018

Abstract: Aluminium-based hybrid metal grid composites (MMC) are extensively utilized in automobile applications (engine cylinders, pistons, etc.) as they exhibit a fantastic blend of properties. Here, a detailed study of nano-mechanical, electrochemical and Raman spectroscopic behavior of friction stir processed Al6061-SiC-graphite hybrid surface composite is presented. The effect of various tool rotational speeds was evaluated along with the monitoring of variation in axial force. Microstructural changes with various tool rotational speeds are studied by using a scanning electron microscope. Raman spectroscopy and X-Ray diffraction studies are used for the spectroscopic characterization of the fabricated hybrid and mono surface composites. Residual stresses and various crystal structure disorders of reinforcement result in the significant change in intensity and a considerable shift in Raman peak positions. The nano-mechanical behavior of the fabricated composite with various reinforcements and tool rotational speeds are analyzed by using nano-indentation. The nano-mechanical behavior of hybrid composite fabricated with an optimum set of processing parameters is superior to mono composites fabricated with the same processing parameters. Also, the electrochemical behavior of the fabricated composites is studied by linear potentiodynamic polarization test. The Al6061-SiC-graphite hybrid surface composite reveals excellent nano-mechanical and electrochemical behavior when fabricated with an optimum set of processing parameters. The tool rotational speed has a pronounced effect on the dispersion of agglomerates and grain refinement of the matrix material. The processing parameters extensively affect the Raman spectroscopic behavior of the hybrid composite. The hybrid surface composite shows better corrosion resistance than the mono composites when fabricated with an optimum set of processing parameters. Reduced intergranular as well as interfacial corrosion pits in hybrid composites increased its resistance to corrosion.

Keywords: hybrid composite; nano-mechanical; corrosion; friction stir processing; Raman spectroscopy

1. Introduction

Aluminum-based hybrid metal grid composites (MMC) are widely utilized in automobile applications (engine cylinders, pistons, etc.) as they exhibit high strength, wear resistance, abrasion resistance, chemical stability, and dimensional stability at high temperature [1,2]. Friction stir processing (FSP) is a solid-state processing strategy used for the fabrication of surface composites. FSP was first established by Mishra et al. to impart high strain rate superplasticity to 7075 aluminum

alloy [3]. In FSP, a non-consumable rotating cylindrical tool with a shoulder and probe is plunged into a substrate and then traversed along the surface of the workpiece. The frictional heat is generated by the rubbing action of tool shoulder with the substrate and softens the material under the shoulder. The material under the shoulder also undergoes plastic deformation due to the high strain rate provided by the stirring action of the tool pin. The main applications of FSP for microstructural modification in metals include homogenization of reinforcement in MMCs [4], grain refinement through dynamic recrystallization [5–7], and superplasticity [8–11].

The Al-SiC surface composites fabricated via FSP reveal better mechanical properties than unreinforced Al alloy. A significant improvement of hardness with SiC reinforcement in Al matrix is observed by various researchers [12–15]. The higher hardness of the Al-SiC mono composite is mainly attributed to grain refinement during FSP and the homogeneous distribution of SiC particles in the Al matrix [13–17]. The friction stir processed composite shows a considerable increase in hardness with the increase in the percentage of reinforcement and finer size of particles [12,15]. The corrosion behavior of the Al-SiC composite has been reported contradictorily by different authors. Some of them reported that Al-SiC composite shows better corrosion resistance as compared to Al alloy [18,19], while some of the authors reported low corrosion resistance in the case of Al-SiC composite as compared to Al alloy [20–22]. The finer size of SiC particles has better corrosion resistance as compared to the bulky particles [18–20]. Corrosion resistance is also improved with the increased volume fraction of SiC particles [18,19,22].

On the other hand, a graphite reinforced Al metal matrix composite shows an excellent wear and tribological properties [23]. Graphite reinforcement in Al matrix decreases the hardness, friction coefficient and coefficient of thermal expansion [24] while wear resistance increases considerably in comparison to the un-reinforced Al alloy [17,23,25,26]. The graphite provides a solid layer of lubricant between the composite and counter hard surface [27]. This graphite layer helps to increase the wear resistance of the composite. However, Modi et al. [21] show that the graphite has a pronounced effect on the corrosion properties of the Al-graphite composite fabricated through the liquid metallurgy route. The increased rate of H_2 evolution due to the high conductivity of graphite leads to a shifting of the corrosion potential of Al-graphite composite in an active direction. Also, the porous nature of graphite leads to sucking of electrolyte in the localized region and increases the corrosion current density, which ultimately increases the corrosion loss. Saxena et al. [28] have also shown in their work that graphite reinforcement leads to higher corrosion loss than the base alloy and aluminum due to the cathodic behavior of graphite particles relative to a matrix, which leads to increased rate of galvanic corrosion. It is also reported that the graphite/Al matrix interface is the preferential site for the nucleation of corrosion in the Al-graphite composite [21,29].

Hybrid MMCs are engineering materials fabricated by reinforcing a substrate with a mixture of two or more different types/forms of particles to achieve the combined advantages of both of them. It was reported in many works that the hybrid composite of Al-SiC-graphite exhibits better wear resistance than those reinforced only with SiC or graphite [30,31]. However, the nanomechanical and electrochemical behavior of Al-SiC-graphite hybrid composite when fabricated through FSP have not been studied to date. Also, the effect of the presence of SiC particles on graphite morphology has never been studied by any research group.

The objective of the present investigation is to study the effect of tool rotational speed on the nanomechanical and electrochemical behavior of both mono (Al-SiC & Al-graphite) and hybrid composite (Al-SiC-graphite). The spectroscopic analysis is also to be conducted to study the morphological change of graphite due to the presence of SiC reinforcement in the hybrid composite.

2. Materials and Methods

An Al6061 plate of 6 mm thickness is used as a substrate material. SiC powder (~100 μm, Alfa Aesar, Haverhill, MA, USA) and graphite powder (~44 μm, Alfa Aesar, Haverhill, MA, USA) are used as a reinforcement for both mono and hybrid composite (SiC: Graphite ~1:1). The microstructure

of all the raw materials is shown in Figure 1a–c. A viscous solution of reinforcement and polyvinyl alcohol (5 wt %) was prepared in the magnetic stirrer (Remi, 5MLH Plus, Remi Lab World, Maharashtra, India) at 1000 rpm and 70 °C. It is then filled in the grooves (3 mm × 2 mm) on Al substrate (Figure 2a). The filled grooves are then allowed to dry in a vacuum drying oven at 120 °C for 4 h. Friction stir welding (ETA Technology, Bangalore, India) inbuilt with strain gauge setup for force measurement was used to carry out FSP on the filled grooves by using an H13 tool of 25 mm diameter flat shoulder with a square pin (5 mm × 5 mm × 5 mm) (see Figure 2b) at various tool rotational speeds of 1800 rpm, 2200 pm, and 2500 rpm. The constant tool traverse speed of 25 mm/min was used for all the experiments. Shoulder plunge depth is varied as 0.2, 0.3 and 0.4 mm for 1800 rpm, 2200 rpm, and 2500 rpm, respectively. It was noticed that many researchers reported the poor distribution of reinforcement particles at tool rotational speeds of around 1800 rpm [32–34]. Thus, to homogenize and study the particle dispersion, high tool rotational speeds were selected in the present study.

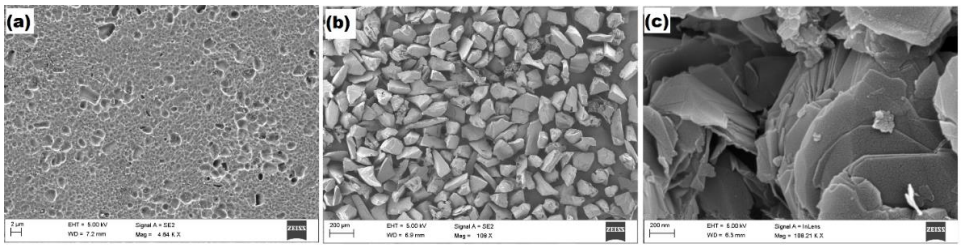

Figure 1. Scanning electron microscopy (SEM) micrographs of as-received (**a**) Al6061, (**b**) SiC powder, and (**c**) graphite powder.

The nanomechanical behavior of the mono and hybrid composite was studied by using a nano-triboindenter (using Hystiron, TI 950, Hysitron, Inc., Minneapolis, MN, USA) under a load of 5000 μN with 10 s time for loading, dwelling and unloading, respectively. Electrochemical behavior was analyzed by linear potentiodynamic polarization test (by using Biologic, SP150, Bio-Logic Science Instruments, Seyssinet-Pariset, France) under 3.5 wt % NaCl solution as an electrolyte. The Tafel fit was carried out for obtaining the values of corrosion current and potential. Raman spectroscopy (using Jobin Yvon Horiba, T64000, HORIBA, Ltd., Kyoto, Japan) was used to study the morphology of graphite and SiC before and after FSP. Microstructural characterization was conducted by scanning electron microscopy (Zeiss) at 5–20 kV. Phase study was carried out by using X-ray diffraction (by using PANalytical XPERT PRO (Malvern Panalytical Ltd., Royston, UK)) with CuKα of 2θ range 20°–120°), and the obtained data were analyzed with X-pert Highscore software to get the different phases formed in the composite.

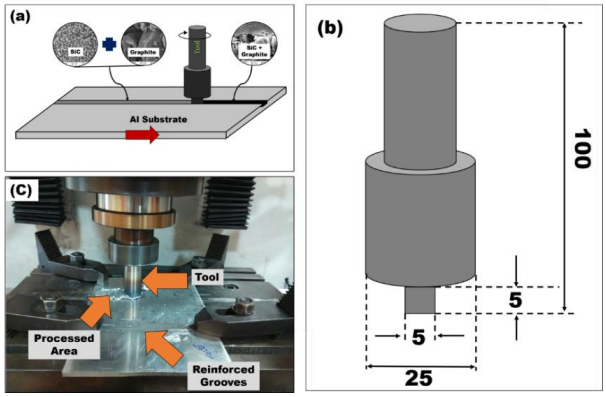

Figure 2. Schematic representation of (**a**) grooved Al6061 sheet for reinforcement, (**b**) friction stir process (FSP) tool, and (**c**) processing setup.

3. Results and Discussions

3.1. Axial Force Variation

The axial force applied during the fabrication of various composites affects the machine setup and tool geometry severely. Thus, a critical assessment is required for its variation with tool rotational speed and type of reinforcement. Figure 3a show the generalized curve obtained while processing unreinforced Al 6061. The overall processing consists of three regions where axial force assessment is necessary, namely (a) plunging, (b) dwelling, and (c) traversing. During plunging, a rotating tool comes in contact with the substrate material and keeps on penetrating until the tool shoulder starts rubbing against the substrate material. Due to the resistance provided by the sudden substrate jump (peak load), the axial force is observed. Plunging is immediately followed by a dwelling of very short duration. The material under the shoulder gets heated up during this phase due to the high friction generated between the tool shoulder and substrate. This heating due to friction softens the base metal, and the axial force decreases to almost 40% of peak load. In the traversing phase, the relative linear movement between tool and shoulder takes place. Subsequently, force attains a steady value during further processing.

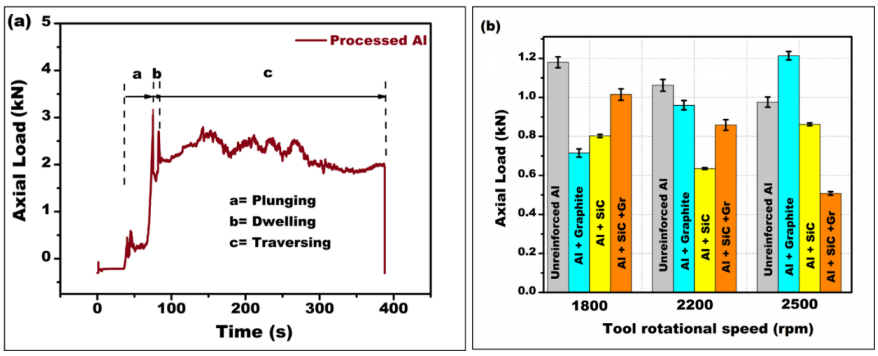

Figure 3. Axial load variation: (**a**) Axial load vs. time curve for non-reinforced processed Al6061 at 2200 rpm; (**b**) axial load vs. tool rotational speed for different reinforcements. Graphite is abbreviated as Gr.

Figure 3b show the mean axial force obtained at various tool rotational speeds for various reinforced composites. The mean axial force in the case of un-reinforced Al decreases with the increase in tool rotational speed from 1800 rpm to 2500 rpm. This decrease in force is attributed to the decrease in material flow stress at elevated temperature, while in the case of Al-graphite mono composite, an opposite trend is noticed. This opposite trend is attributed to the (a) very high thermal conductivity of graphite, and (b) the reduction in coefficient of friction (COF) between the FSP tool and Al substrate by graphite. The high thermal conductivity of graphite is partially responsible for the increase in mean axial force with an increase in tool rotational speed. Due to the high thermal conductivity possessed by graphite, the heat generated at the tool–metal interacted surface transferred rapidly to the area just ahead of the processing point and softens this area. Thus, a cyclic interaction of tool with hard and soft zones takes place which results in a severe variation of force during traversing and ultimately increases mean axial force. The graphite has an interlayer shear strength of ~0.48 MPa, which is less than the flow stress of Al during FSP. Due to such low interlayer shear strength of graphite, it is sheared out on the Al surface in the form of a very thin layer during FSP. This thin layer acts as a solid lubricant and reduces the COF between the FSP tool and Al substrate, and hence the seizure could not take place during processing, thereby affecting the material flow and axial force during FSP [14]. This effect becomes more pronounced at higher tool rotational speeds, and thus peak axial thrust is observed at 2500 rpm. However, the variation with tool rotational speed is the same as that of un-reinforced Al alloy.

The axial force variation in Al-SiC mono composite is very random. The force of ~0.8 kN is observed at a tool rotational speed of 1800 rpm, which increases to ~0.6 kN at 2200 rpm and further increases to ~0.9 kN at 2500 rpm. The higher axial force at 1800 rpm is due to the insufficient material flow during FSP. The material flow increases at 2200 rpm due to higher heat generation. At 2500 rpm, excessive heat is generated which reduces the flow stress of aluminium. Due to this reduction in flow stress, the fragmentation of SiC particles into smaller pieces is significantly reduced. Instead of fragmenting into smaller pieces, the large particles flow along with the material and during this phenomenon come in contact with the FSP tool and increase the force.

In Al-SiC-graphite hybrid composite, the axial force consistently decreases from 1800 rpm to 2500 rpm. The severe fluctuations which are observed in Al-graphite mono composite does not arise here due to the presence of hard abrasive SiC particles. These SiC particles assist in the seizure between the FSP tool and Al matrix even in the presence of graphite. As explained earlier, in Al-SiC mono composite at 2500 rpm tool rotational speed, the heat generated is excessive, due to which flow stress decreases significantly and fragmentation of SiC particles could not take place resulting in high axial thrust. However, in Al-SiC-graphite hybrid composite, owing to the high conductivity of graphite, the excessive heat generated is transferred quickly to neighbouring regions, and thus the considerable value of flow stress is maintained during processing. This higher flow stress enables the fragmentation of SiC particles into smaller pieces. Thus, the high conductivity of graphite along with the presence of hard abrasive SiC particles explains the force variation obtained in Figure 3b.

3.2. Raman Spectroscopy

Raman spectroscopy is an important characterization technique to investigate the structure and morphology of various carbonaceous reinforcement. Figure 4 represents the Raman spectrum obtained for various raw materials and fabricated composites, respectively. The raw graphite powder shows three broad peaks at 1340 cm^{-1} (D band), 1573 cm^{-1} (G band) and 2700 cm^{-1} (2D band). The peak identified at 1573 cm^{-1} is known as G band and is an outcome of C-C in-plane vibrations. The size of the G band corresponds to the crystalline quality of the carbonaceous compound [35]. The Raman peak observed at 1340 cm^{-1} is a result of single phonon scattering and the interaction of the electron with imperfection. It is termed as the D band or defect band. The intensity of the D band signifies the degree of disorder present in the crystal structure [35,36]. The Raman peak at 2700 cm^{-1} corresponds to the two-phonon scattering mode and is known as a 2D band. The 2D band signifies the degree of graphitization present in the structure [37,38].

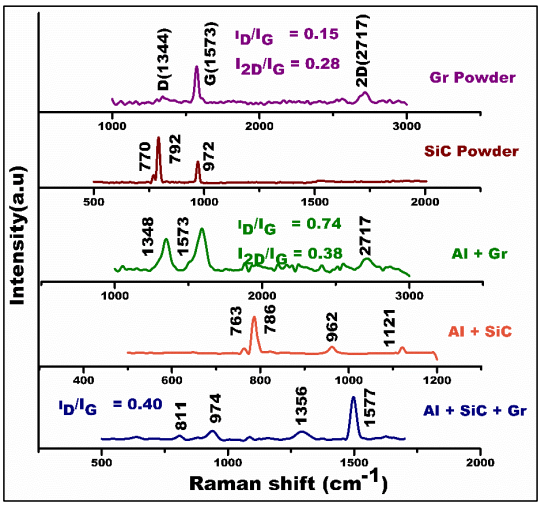

Figure 4. Raman spectrum of powder and various composites fabricated at 2200 rpm. Graphite is abbreviated as Gr.

During FSP, graphite present in the composite is strained and the interatomic distance between the layers changes. This phenomenon introduces compressive residual stresses in the graphite and distorts its hexagonal symmetry. This behavior is identified by the low-intensity G band in processed samples. The increase in the D band intensity of Al-graphite composite corresponds to (i) an increase of the unorganized amount of carbon in the sample, and (ii) a reduction in the graphite crystal size [39].

The ratio of D to G band intensity (I_D/I_G) increased from 0.15 in powder sample to 0.74 in Al-graphite mono composite, while the corresponding value for the hybrid composite is 0.40. This increase in the ratio signifies the increased amount of disorder in the composites as compared to the graphite powder sample [40]. FSP at 2200 rpm increases the edge-related disorder of graphite and consecutively the amount of randomly oriented graphite crystals also increases. As the D band intensity straightforwardly resembles the level of imperfection, it increases in the composites. The combined effect of the above two phenomena results in the higher I_D/I_G ratio of Al-graphite composite, while in case of the hybrid composite, the presence of hard abrasive SiC particles restricts the edge disorder of graphite during processing. Thus, the low value of the I_D/I_G ratio is justified in the hybrid composite. The processing also tends to reduce the graphite crystal size, and thus the intense peak of the D band is justified in the composites. Tunistra and Koenig [39] also show that the nature of the D band is dependent on the carbon grain size (L_g) by Equation (1) shown below.

$$\frac{I_D}{I_G} = \frac{C(\lambda)}{L_g\,(\mathrm{nm})},\ C(\lambda = 514.5\,\mathrm{nm}) = 44 \quad (1)$$

From Equation (1), the intensity of the D band is inversely related to the carbon grain size. The grain refinement justifies the intense peak of D band in the processed Al-graphite composite due to friction stir processing. The 2D band intensity corresponds to the number of graphene layer exhibits in the structure [41]. The intensity ratio I_{2D}/I_G increases from 0.28 in powder sample to 0.38 in the composite. This increase in (I_{2D}/I_G) proportion corresponds to the disintegration of graphite and exfoliation of graphitic layers because of amplified residual stresses among the neighboring graphene layers during processing.

Figure 4 also show the Raman spectrum of SiC component in both powder and composites. The Raman peaks corresponding to SiC in the range 500–1000 cm^{-1} indicate the defects/disorder in the crystal lattice, lattice strain, impurities, and mobility. The present Raman spectra show three characteristic features: the peaks of E2 symmetry at ~770 and ~792 cm^{-1} correspond to TO(Γ) phonon or transverse optic mode, and the low-intensity peak of A1 ~972 cm^{-1} corresponds to LO(Γ) phonon or longitudinal optic mode. These three characteristic features confirm the presence of SiC in 6H-SiC polytypes [21]. The high-intensity peaks at ~770 cm^{-1} and ~792 cm^{-1} correspond to the Si-C bond [21]. The peak observed at ~972 cm^{-1} resembles the second order band of silicon.

It is observed that the width and intensity of the TO peak analogous to ~790 cm^{-1} in the case of powder sample is ~50 cm^{-1} and ~2100 au (arbitrary unit), respectively, while in the case of processed samples the values change to ~40 cm^{-1} and ~6000 au, respectively. The sharper and more intense TO peak in the case of the processed sample is ascribed to the high temperature generation during processing [22]. It is perceived that the LO(Γ) peak intensity is reduced from ~1665 au in powder sample to ~1040 au in the processed samples. This is attributed to the heating effect produced during the processing. The downshift in the peaks is observed in the first as well as second order bands of Al-SiC composite as compared to SiC powder sample. This downshift is attributed to the high temperature generation during friction stir processing [23]. The higher temperature leads to thermal expansion and strain being induced due to lattice incompatibility by the other phonons [23].

3.3. X-Ray Diffraction

Figure 5 reveals the X-ray Diffraction (XRD) plots of as-received fine particles and processed specimens, respectively. The major peaks of Al are obtained at 38.3°, 44.6°, 65.1°,78.2° and 82.5° corresponding to the (111), (200), (220), (311) and (222) planes of Al. The minor intensity peak at 26.54°

in graphite reinforced mono composite and hybrid composite causes the surety of graphite content in the samples. This low-intensity peak corresponds to the (002) plane of carbon [42]. The major peaks of SiC in powder samples were observed at 35.65°, 38.07°, 59.99°, 71.78° and 75.51°, while in composites they were observed at 35.65° and 75.51°. The planes associated with these angles are (111), (200), (220), (311) and (222), respectively. However, the SiC 200 and other small intensity peaks are not present. There are a couple of potential reasons for the non-existence of SiC (200) peak and other peaks of low intensity in the processed samples. Firstly, due to the lower volume fraction of SiC, it is more likely that lower intensity reflections become indistinguishable from noise. Secondly, preferred orientation issues during processing result in decreasing the intensity of SiC (200) relative to other planes [43]. Lastly, Al possesses high-intensity peaks (~2500 au) due to its highly crystalline nature while the intensity of SiC (200) peaks observed in powder sample are very much less (~38 au). This large difference among the intensities makes the SiC (200) peaks indistinguishable from noise. Also, due to the less crystalline behavior of SiC than Al, the long-range order for a specific set of indices is lost. It is visible from the graphs that no new phases (Mg_2Si or Al_4C_3) were formed except the added reinforcement powders, i.e., SiC and graphite. Witnessing no shifting of the peaks in the graphs with the reinforcements, it can also be inferred that no chemical reaction happened between the reinforcements SiC and graphite powders during FSP, and thus there is no chance of formation of any intermetallic compound. During fabrication of the Al-carbonaceous compound composite, the carbonaceous compound reacts with Al at grain boundaries and forms Al_4C_3. This phenomenon becomes the point of brittle weakness and leads to poor mechanical properties. However, the kinetics of this reaction start at a temperature above 500 °C [44]. Since FSP is a solid-state processing strategy, the temperature rise during the processing ranges from 400–500 °C [45,46]. Thus, Al_4C_3 formation is avoided due to the unavailability of the temperature required for the start of a reaction between Al and carbon. This effect presents an advantage of friction stir processing over other alloying methods such as thermal spraying, laser beam, and powder metallurgy routes. In these processes, the rise in temperature beyond the melting point can lead to the formation of different chemical compounds by the reaction of the reinforcement particles among themselves which is harmful to the properties of the desired composite [47].

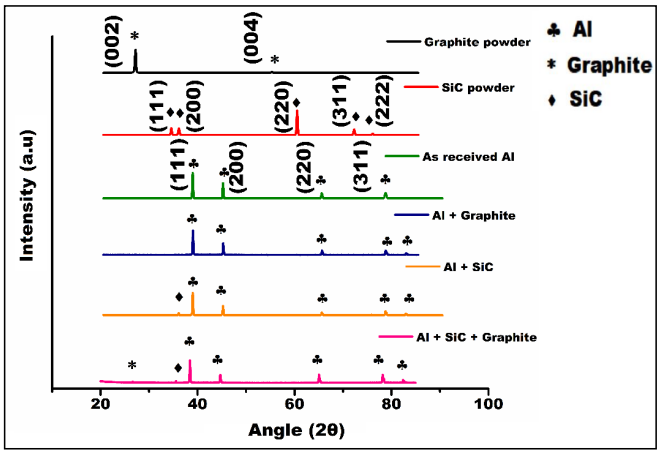

Figure 5. X-ray Diffraction (XRD) micrographs of as-received samples and friction stir processed samples.

3.4. Electrochemical Behaviour

Figure 6a–c shows the linear potentiodynamic polarization test results conducted to analyze the electrochemical or corrosion behavior of various mono and hybrid composites fabricated at various tool rotational speeds. The corrosion potential (E_{CORR}) and corrosion current densities (I_{CORR}) obtained by using Tafel extrapolarization at various tool rotational speeds are shown in Table 1. Figure 6d show

the corrosion rate obtained with various composites at different processing parameters. The corrosion rate (CR) is calculated using the equation

$$\mathrm{CR} = \frac{I_{\mathrm{CORR}} \cdot K \cdot \mathrm{EW}}{d \cdot A} \tag{2}$$

where CR is in millimeter per year (mmpy); I_{CORR} is corrosion current (in A); K is the constant that defines the units of the corrosion rate. It should be 3272 mm/(A·cm·year) for CR to be in mmpy; EW is equivalent weight (in gm/equivalent); d is density (in g/cm^3); and A is sample area (in cm^2).

As shown in Figure 6, the addition of reinforcements along with FSP shifts the corrosion potential (E_{CORR}) in a more active direction, with hybrid composite being more active than the mono composites.

Table 1. The potentials and current densities obtained by Tafel extrapolarization analyses for as-received Al6061 and various composites fabricated at different tool rotational speeds.

Material	Tool Rotational Speed (RPM)	E_{CORR} (mV)	I_{CORR} (μA/cm^2)
As-received Al	-	−707.37	1.77
As-processed Al	1800	−715.95	1.06
	2200	−722.68	1.59
	2500	−722.11	1.14
Al-SiC	1800	−741.95	1.83
	2200	−718.79	1.37
	2500	−739.39	1.48
Al-graphite	1800	−754.01	1.80
	2200	−754.30	1.85
	2500	−754.23	1.81
Al-SiC-graphite	1800	−760.29	1.60
	2200	−751.59	0.92
	2500	−759.65	1.24

The Al-SiC mono composite fabricated at 1800 rpm shows higher corrosion current density (I_{CORR}) as compared to base alloy. The higher I_{CORR} at 1800 rpm is attributed to the presence of bulky SiC particles and coarse grain structure which provides the potential cathodic sites for the electrolyte (see Figure S1 in Supplementary Materials). At these sites, the corrosion pits initiate and progress. The bulk SiC particle also leads to the breakdown of the Al_2O_3 layer formed on the matrix, which alloys the contact between the electrolyte and matrix. This contact between electrolyte and composite ultimately increases the corrosion loss of the composite. At 2200 rpm, the optimum combination of grain size, particle size and uniform distribution of SiC particles leads to the minimum I_{CORR}. At a higher tool rotational speed of 2500 rpm, grain coarsening due to high-temperature generation takes place [48]. This grain coarsening increases the corrosion loss even though the particles are more uniformly distributed in the matrix. The grain boundaries act as the cathodic sites for the galvanic corrosion, and thus grain coarsening leads to an increase in corrosion loss [18].

In the case of Al-graphite mono composite, maximum corrosion loss was observed as compared to various fabricated composite and unreinforced Al6061. The various oxidation and reduction reaction taking place on the Al surface are shown by Equations (3)–(6), respectively.

$$O_2 + 4H^+ + 4e^- = 2H_2O (E_{\mathrm{REV}} = 0.82 V_{\mathrm{SHE}}) \tag{3}$$

$$Al^{3+} + 3e^- = Al (E_{\mathrm{REV}} = -1.66 V_{\mathrm{SHE}}) \tag{4}$$

$$2H^+ + 2e^- = H_2 (E_{\mathrm{REV}} = -0.41 V_{\mathrm{SHE}}) \tag{5}$$

$$Al^{3+} + 3e^- = Al\ (E_{\mathrm{REV}} = -1.66 V_{\mathrm{SHE}}) \tag{6}$$

As seen from the above equations, there is a wide difference between the reversible potential (E_{REV}) for the reactions. This wide difference in reversible potentials leads to the formation of galvanic coupling between matrix and reinforcement. Reinforcement acts as an inert electrode upon which O_2 and H^+ reduction occur [49]. The shifting of E_{CORR} towards more negative values and the increase in I_{CORR} signifies the activation of aluminium by the presence of graphite [23,28]. Increased evolution of H_2 due to the highly conducting nature of graphite shifts the corrosion potential of Al/graphite mono composite into a more active direction than the as-received Al6061 [28]. The cathodic nature of graphite in NaCl solution is also responsible for the galvanic corrosion of the composite [49]. This cathodic behavior of graphite leads to the formation of a localized galvanic cell, in which graphite particles act as a cathode and lead to the anodic dissolution of Al in the chloride solution [23,28]. These localized galvanic cells break the layer of Al_2O_3, and pitting of Al matrix is initiated. The grain boundaries and reinforcement–matrix interface also act as potential sites for galvanic cell formation [29]. This discussion concludes with the fact that the primary mechanism of corrosion in Al-graphite composite is galvanic corrosion, whereas the H_2 evolution and intergranular corrosion contribute towards the increased corrosion loss.

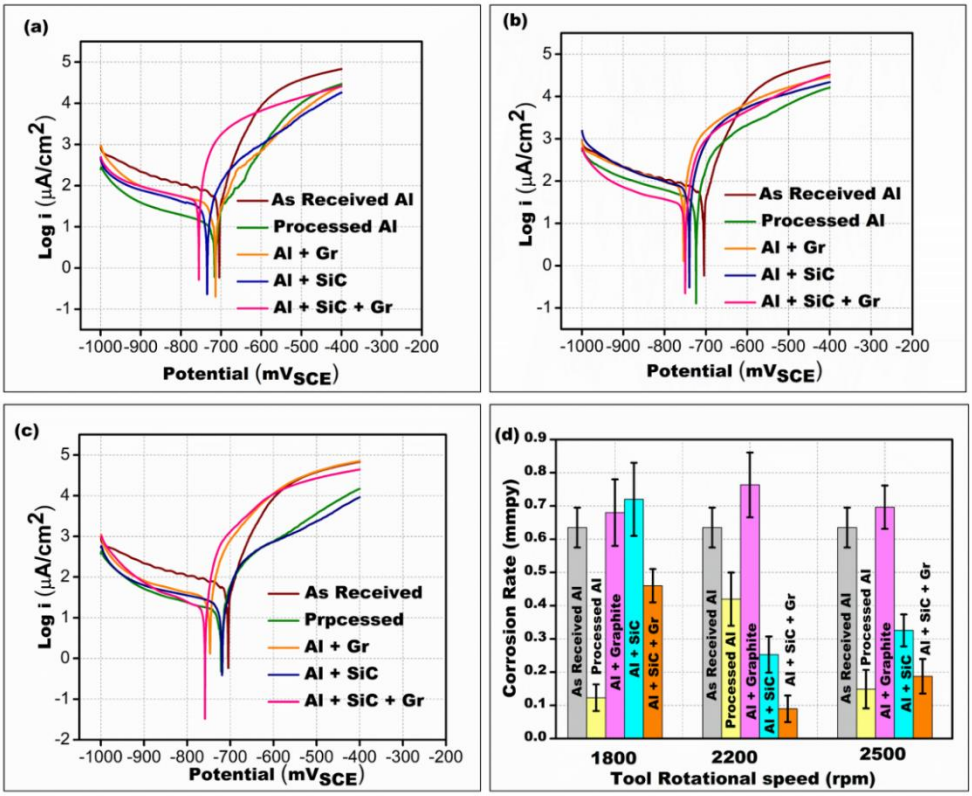

Figure 6. Linear potentiodynamic polarization curves obtained at (**a**) 1800 rpm (**b**) 2200 rpm (**c**) 2500 rpm; (**d**) corrosion rate. Graphite is abbreviated as Gr.

The minimum corrosion loss is noticed in Al-SiC-graphite hybrid composite fabricated at 2200 rpm tool rotational speed, as shown in Figure 6b. Hybrid composite fabricated at 2200 rpm contains graphite in both particles as well as in layer form (Figure 7d,f). This behavior accomplishes two functions: (i) the reduction of galvanic corrosion due to the less concentrated graphitic region in the absence of particle form; and (ii) the protection of Al matrix from electrolyte due to the formation of a layer over the matrix. With the reduction in particle form of graphite, the interfacial corrosion is also reduced due to a decrease in the number of potential cathodic sites. The crevice corrosion between Al and SiC interface is also reduced due to the presence of a graphite layer between them. Increased grain refinement at 2200 rpm also reduces the possibilities of intergranular corrosion. This combined effect ultimately

reduces the corrosion loss of the hybrid composite fabricated at 2200 rpm drastically. The higher corrosion loss at 1800 rpm is attributed to the non-uniform distribution of SiC particles due to high flow shear stress in the absence of sufficient heat. The agglomerated particles become the potential sites for the formation of galvanic coupling and increase the corrosion loss. The intermediate value of current density at 2500 rpm was due to the grain growth during processing. However, a uniform distribution and fine particles of SiC and graphite are present. At higher tool rotational speeds, due to severe heat generation, the temperature rises and leads to coarsening of grains as well as chemical coalescence of particles (See Figure S2 in supplementary materials). This coarse grain structure provides the sites for galvanic corrosion.

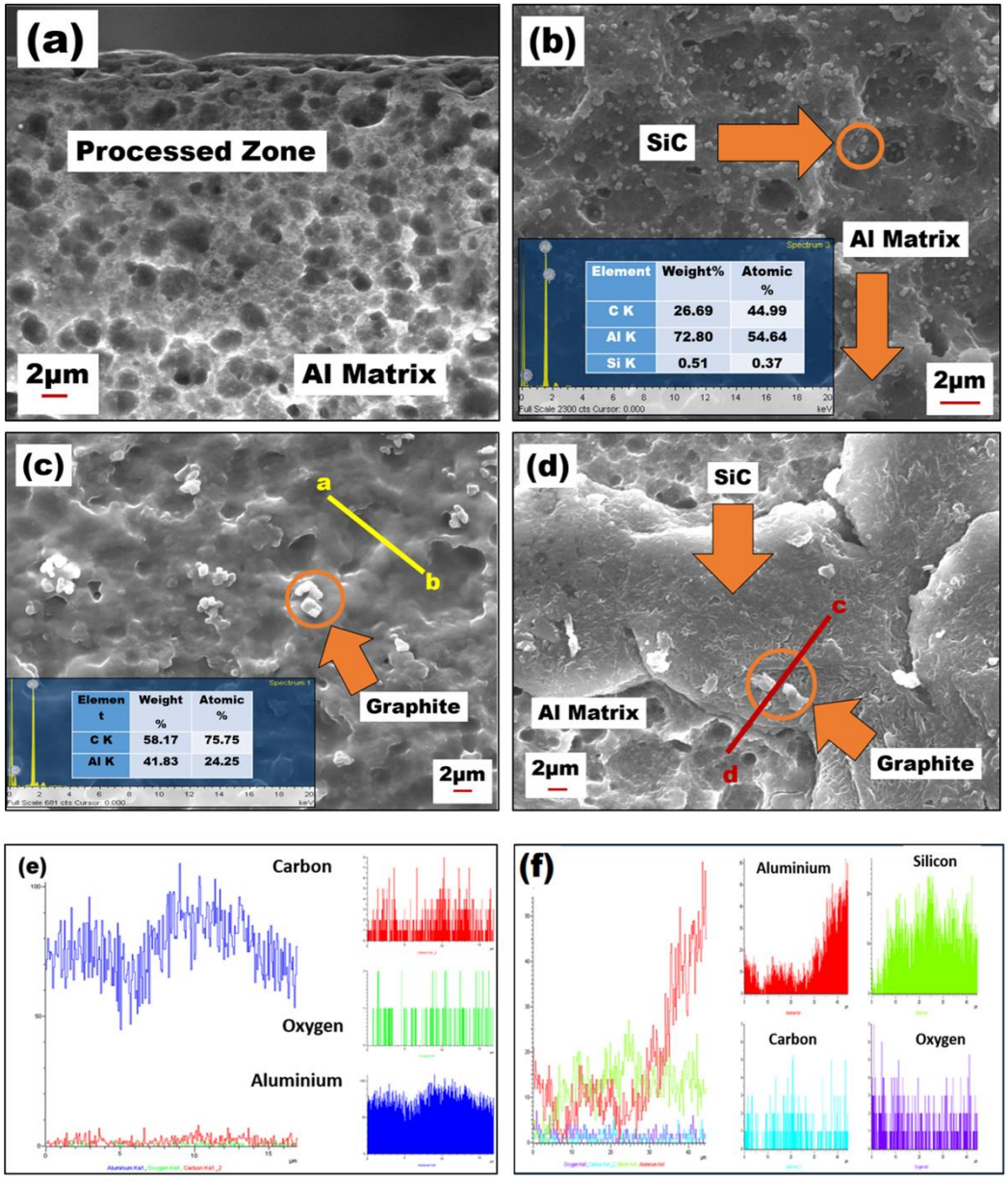

Figure 7. SEM micrographs of (**a**) processed Al, (**b**) Al-SiC mono composite, (**c**) Al-graphite mono composite, (**d**) Al-SiC-graphite hybrid composite, (**e**) line energy dispersive X-ray spectroscopy (EDX) analysis of a-b, (**f**) line EDX analysis of c-d.

3.5. Microstructural Characterization

Figure 7a–d show the scanning electron microscopy (SEM) micrographs of various composites fabricated at a tool rotational speed of 2200 rpm. Since the best mechanical and electrochemical properties are obtained at 2200 rpm, the micrographs of composites fabricated at 2200 rpm are only shown here. The presence of various reinforcements is confirmed by energy dispersive X-ray spectroscopy (EDX) analysis at corresponding points. Figure 7a shows the refined grain structure of unreinforced Al after processing. The homogeneous distribution of SiC reinforcement along with some coarse particles and refined grains can be visualized in the Al-SiC mono composite, as shown in Figure 7b. The presence of SiC particles is also confirmed by EDX analysis (inset). The presence of graphite in both layer and particle forms is noticed in the Al-graphite mono composite, as shown in Figure 7c. This phenomenon is attributed to the plastic deformation at high tool rotational speed, which squeezes out the graphite and distributes it uniformly over the Al matrix.

The point EDX (inset) on the encircled region and line EDX at a-b (Figure 7e) confirm the presence of graphite in both particle as well as layer form, respectively. The presence of oxygen in line EDX at a-b signifies the formation of an Al_2O_3 layer on the matrix. Figure 7d shows the SEM micrograph of Al-SiC-graphite hybrid composite. Here also, the graphite is present in both particle and layer form. The line (c-d) EDX analysis shown in Figure 7f confirms the presence of both the reinforcements along with Al_2O_3 layer on the matrix. The grain size in all the above three fabricated composites is nearly the same.

Figure 8a–d show the SEM micrographs of the as-received Al sample, Al-SiC mono composite, Al-graphite mono composite and Al-SiC-graphite hybrid composite after the potentiodynamic polarization test. The cathodic reaction for Al in aerated near neutral ph solution is oxygen reduction which is later followed by adsorption, i.e.,

$$\frac{1}{2}O_2 + H_2O_{(s)} + e^- = OH_{ads.} + OH^- \quad (7)$$

$$OH_{ads.} + e^- = OH^- \quad (8)$$

At the same time, the anodic reaction of Al starts from a corrosion potential of −707.3 mV with an average current density of 1.77 $\mu A/cm^2$. During the anodic reaction, a layer of aluminium oxide is formed on the surface according to the reaction

$$Al_{(s)} + 3OH^- = Al(OH)_{3,ads.} + 3e^- \quad (9)$$

$$Al(OH)_{3,ads.} = Al_2O_3.3H_2O \quad (10)$$

This layer of oxide is composed of an adherent, compact and stable inner layer while the outer layer is porous and less stable and thus more favorable for the corrosion [23]. Due to this phenomenon, an abrupt increase in current is observed (Figure 6) after increasing the applied potential. This increase in current leads to the attack of chloride ions on the flawed oxide layer, and a breakdown of the passive layer takes place which ultimately results in the pitting corrosion [50]. The reactions involved in this phenomenon are as follows:

$$Al = Al^{3+} + 3e^- \quad (11)$$

$$Al^{3+} + 4Cl^- = AlCl_4^- \quad (12)$$

This phenomenon explains the corrosion pits formed on the aluminium surface, as shown in Figure 8a. A sharp pitting region in the case of Al-SiC composite can be seen from the potentiodynamic curves in Figure 6b. Also, Figure 8b shows corrosion pits near the SiC particle. It was reported that Al-SiC mono composite is more susceptible to the corrosion pits than the unreinforced alloy [21]. The inhibiting quality of SiC particles to progress the growth of the pit is the reason behind this more corrosion-prone behavior [51]. The SiC particles cause the breakdown of the oxide film and provide the

path for chloride ions to come in direct contact with the matrix [21]. Thus, the SiC/Al matrix interface becomes the potential site for galvanic corrosion [21]. However, the pit formation does not start at the particle. Instead, it starts from the Si-rich layer around the SiC particle [51]. The fine grain structure due to FSP controls the intergranular corrosion pits to a great extent, and thus the corrosion effect is mainly due to the presence of SiC particles, whereas in the case of as-received Al alloy, the intergranular pitting is the primary reason for higher current density.

Figure 8c shows the SEM micrograph of Al/graphite mono composite after the corrosion test. The interfacial pit at the Al/graphite interface can be seen from the micrograph. Also, the pit density of the Al/graphite mono composite is more than the unreinforced Al alloy. The increased pitting tendency was attributed to the increase in corrosion current due to the evolution of H_2 at the aluminium alloy and over the graphite surface. Drastic H_2 evolution at the graphite surface is due to the higher exchange current density for H^+/H_2 on graphite [28]. This H_2 evolution breaks the oxide layer formed on the surface and leads to galvanic corrosion. The Al/graphite interface is the preferential site for the corrosion pits and galvanic corrosion to occur (Figure 8c).

Figure 8d shows the SEM micrograph of Al-SiC-graphite hybrid composite. It is seen from the micrograph that the presence of SiC and graphite in near periphery reduces the tendency of interfacial pit formation. The reduced intergranular as well as interfacial corrosion pits result in minimum corrosion loss in the case of hybrid composite. Due to the presence of SiC particles, the ratio of graphite present in the form of film is more than that of the particle form. Thus, the H_2 evolution decreases due to the unavailability of a concentrated graphite region and decreases the corrosion loss. This thin film of graphite also protects the matrix from chloride ions contact and avoid unnecessary pitting.

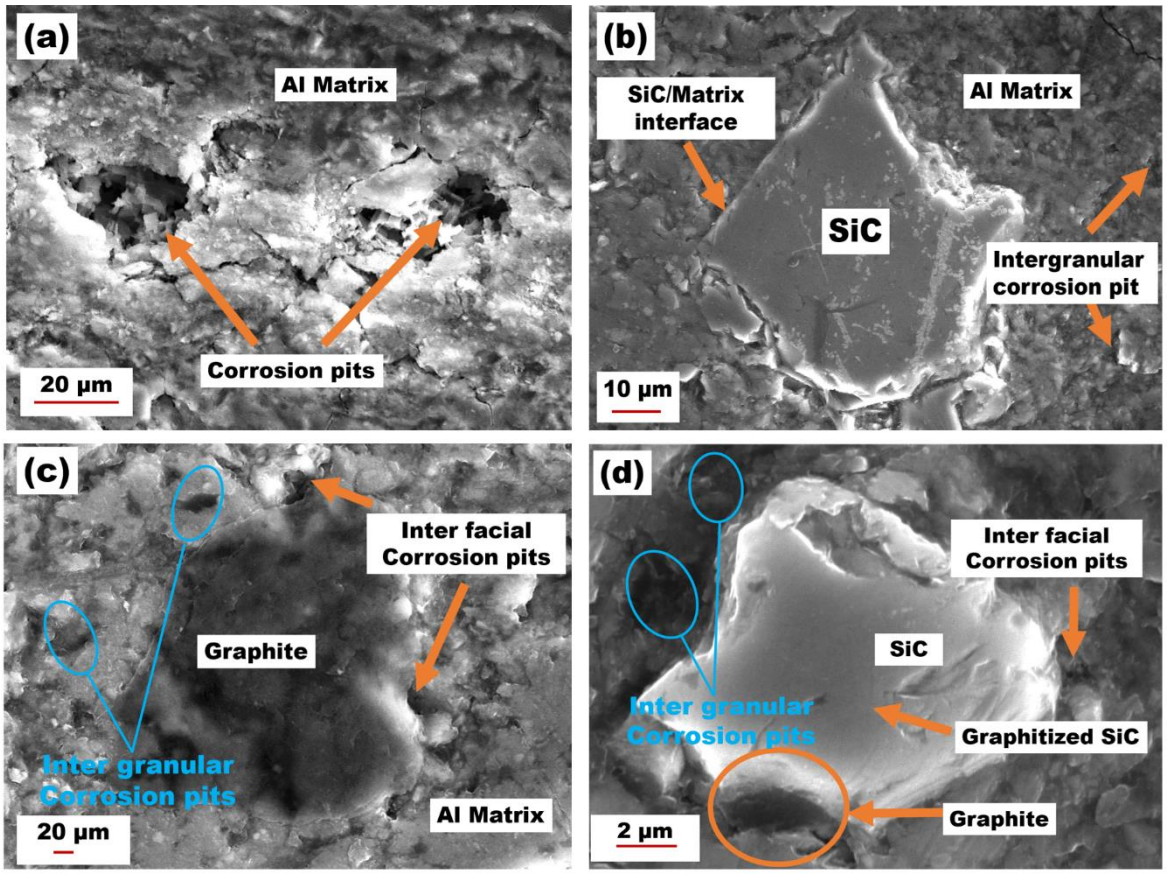

Figure 8. SEM micrographs of composite fabricated at 2200 rpm after potentiodynamic polarization test: (**a**) as-received Al, (**b**) Al-SiC mono composite, (**c**) Al-graphite mono composite, (**d**) Al-SiC-graphite hybrid composite.

3.6. Nanomechanical Behaviour

The nanomechanical behavior of various composites fabricated at 2200 rpm and 2500 rpm tool rotational speeds is studied by using nanoindentation technique. Since the best electrochemical properties are obtained at these parameters, the study is conducted only for the best samples. Figure 9a–c shows the nanoindentation results obtained for the composites fabricated at 2200 rpm. The maximum nano-hardness (0.38GPa) is obtained for Al-SiC composite, whereas Al-graphite mono composite and hybrid composite show nano-hardness values of 0.30 GPa and 0.35 GPa, respectively. The increase in nano-hardness is attributed to the grain refinement due to dynamic recrystallization and the existence of compressive strains in the stir region [52]. Another possible reason for the increase in hardness is the generation of geometrically necessary dislocations (GND). During FSP, the discrepancy between the coefficient of thermal expansion and elastic modulus results in the generation of these GNDs [53]. These GNDs restrict the dislocation movement and contribute towards the higher strength of the composite. The hardness of reinforced abrasive SiC particles also plays a significant role in increasing the nano-hardness of the composite. Figure 9c shows the load-displacement curve (p-h curve) for various composites fabricated at 2200 rpm. The figure visualizes that the resistance to deformation offered by a mono composite of Al-graphite is significantly lower compared to the deformation resistance offered by the Al-SiC mono composite and hybrid composite. The Al-SiC composite obtains the hardest crystallographic plane. This statement is justified by the minimum penetration depth achieved by the Al-SiC composite at the peak load. The nature of the curve obtained with Al-SiC composite show a sudden jump around 4500 µN. This sudden rise in slope can be attributed to the higher stiffness provided by the SiC composite [54].

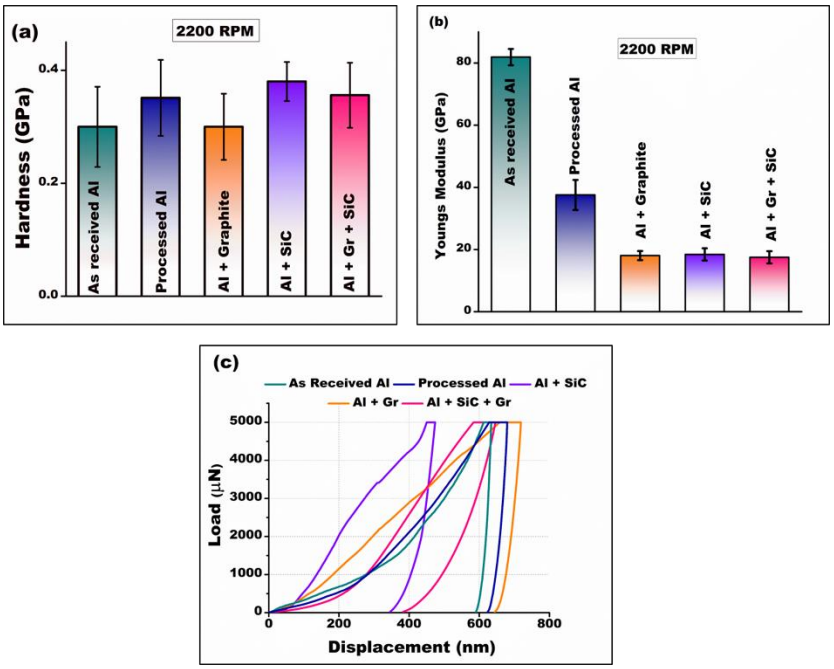

Figure 9. Comparison of (**a**) nano-hardness, (**b**) Young's modulus, (**c**) load vs. displacement curve at 2200 rpm. Graphite is abbreviated as Gr.

Figure 10a–c shows the nano-hardness result obtained for various composites fabricated at 2500 rpm. From the p-h curve, the mono composite of Al-graphite shows greater elastic recovery as compared to other reinforced composites. The hybrid composite shows a pop-in during loading at around 3000 µN loads. This pop-in is the result of debonding between the Al matrix and reinforcement [55]. The twinning effect and slip dislocation also contribute towards this change of p-h

curve around 3000 μN loads. The minimum depth of penetration in Al-SiC composites indicates the higher hardness of the composite [55]. As explained earlier, at 2500 rpm, the grain growth takes place; but at the same time, due to higher heat generation, the particles are more uniformly distributed in the Al matrix. Thus, due to the dominating mechanism of uniform particle dispersion, a higher hardness as compared to the composites fabricated at 2200 rpm is observed. The soft phase of graphite starts early yielding during loading and leads to the lower hardness of the Al-graphite mono composite. This localized yielding is the result of residual stresses due to the shearing of material during FSP [55].

Comparing Figures 9a and 10a, it could be noted that the nano-hardness at a processing speed of 2500 rpm is greater than that at 2200 rpm. Although the hardness values are higher in the case of 2500 rpm, it was observed that the variation in microhardness (see Figure S3 in Supplementary Materials) at different points is severe and lacks uniformity in hardness. On the other hand, samples processed at 2200 rpm shows less hardness but with more uniformity.

Comparing Figures 9b and 10b, it could be noticed that the hardness for the composite is marginally higher than the base metal but that reduced modulus decreased sharply. This phenomenon is attributed to the fact that the modulus is the intrinsic property of the material and strongly depends on the atomic bonding of the material. In the case of as-received material, the atomic bonding is perfect while it gets distorted by the addition of reinforcement and thus modulus gets decreased. However, a similar phenomenon is not observed in the composites fabricated at 2500 rpm because, under high heat and intensified plastic deformation, the Al and reinforcements forms a strong atomic bonding.

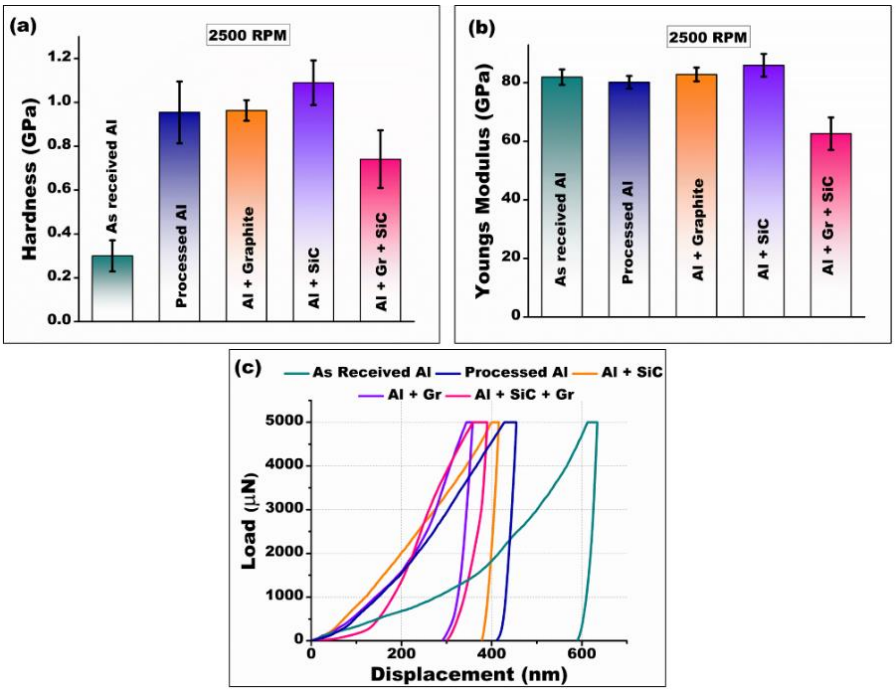

Figure 10. Comparison of (**a**) nano-hardness, (**b**) Young's modulus, (**c**) load vs. displacement curve at 2200 rpm. Graphite is abbreviated as Gr.

4. Conclusions

The hybrid composite of Al-SiC-graphite has been successfully fabricated through FSP. The effect of various process parameters and reinforcement on mechanical properties, electrochemical properties, and the morphology of reinforcement were studied. The main conclusions can be listed as follows:

- The mean axial force during FSP is increased in the case of Al-graphite mono composite due to the high thermal conductivity possessed by graphite;

- The presence of residual stresses in the fabricated composite is confirmed by noteworthy Raman peak shift. The existence of edge disorder in graphite crystal is also noticed. FSP also leads to the exfoliation of graphite towards single-layer graphene;
- The mechanical properties are improved due to particle reinforcement, and optimum uniform properties are obtained at a tool rotational speed of 2200 rpm when processed at 25 mm/min;
- The hybrid composite revealed best electrochemical properties when fabricated at 2200 rpm. The improved corrosion resistance is attributed to the decrease in interfacial and intergranular corrosion due to graphite layer and grain refinement, respectively;
- From XRD analysis, no formation of any intermetallic compounds was observed in any of the composite formulations;
- It could be summarized that the analysis presented herein provides encouraging results for utilizing friction stir processing as a fabrication tool for Al-SiC-graphite hybrid surface composites.

Supplementary Materials: The following are available online at http://www.mdpi.com/2504-477X/2/2/32/s1, Figure S1: SEM micrograph of Al-SiC mono composite fabricated at 1800 rpm, Figure S2: SEM micrographs of various composite, Figure S3: Microhardness variation at cross-section with different reinforcements when processed at various processing speed.

Author Contributions: Abhishek Sharma have designed, synthesized and characterized the composite. Vyas Mani Sharma contributed in the fabrication of Composite using FSP. Baidehish Sahoo and Jomy Joseph contributed in technical writing and data curation. Supervision, manuscript editing, and project administration is carried out by Jinu Paul.

Funding: This research received no external funding.

Conflicts of Interest: The authors declare no conflict of interest.

References

1. Hassan, A.M.; Almomani, M.; Qasim, T.; Ghaithan, A. Effect of Processing parameters on friction stir welded aluminum matrix composites wear behavior. *Mater. Manuf. Process.* **2012**, *27*, 1419–1423. [CrossRef]
2. Basavarajappa, S. Tool wear in turning of graphitic hybrid metal matrix composites. *Mater. Manuf. Process.* **2009**, *24*, 484–487. [CrossRef]
3. Mishra, R.S.; Mahoney, M.W.; McFadden, S.X.; Mara, N.A.; Mukherjee, A.K. High strain rate superplasticity in a friction stir processed 7075 Al alloy. *Scr. Mater.* **1999**, *42*, 163–168. [CrossRef]
4. Berbon, P.B.; Bingel, W.H.; Mishra, R.S.; Bampton, C.C.; Mahoney, M.W. Friction stir processing: A tool to homogenize nanocomposite aluminum alloys. *Scr. Mater.* **2001**, *44*, 61–66. [CrossRef]
5. Karthikeyan, L.; Senthilkumar, V.S.; Balasubramanian, V.; Natarajan, S. Mechanical property and microstructural changes during friction stir processing of cast aluminum 2285 alloy. *Mater. Des.* **2009**, *30*, 2237–2242. [CrossRef]
6. Li, J.L.; Xiong, Y.C.; Wang, X.D.; Yan, S.J.; Yang, C.; He, W.W.; Chen, J.Z.; Wang, S.Q.; Zhang, X.Y.; Dai, S.L. Microstructure and tensile properties of bulk nanostructured aluminum/graphene composites prepared via cryomilling. *Mater. Sci. Eng. A* **2015**, *626*, 400–405. [CrossRef]
7. Mahmoud, T.S. Effect of friction stir processing on electrical conductivity and corrosion resistance of AA6063-T6 Al alloy. *Proc. Inst. Mech. Eng. Part C J. Mech. Eng. Sci.* **2008**, *222*, 1117–1123. [CrossRef]
8. Mishra, R.S.; Mahoney, M.W. Friction stir processing: A new grain refinement technique to achieve high strain rate superplasticity in commercial alloys. *Mater. Sci. Forum* **2001**, *357*, 507–514. [CrossRef]
9. Patel, V.V.; Badheka, V.; Kumar, A. Influence of friction stir processed parameters on superplasticity of Al-Zn-Mg-Cu alloy. *Mater. Manuf. Process.* **2016**, *31*, 1573–1582. [CrossRef]
10. Verdera, D.; Valle, J.A.; Rey, P.; Gesto, D.; Fernández, A.; Ruano, Ó.A. Effect of friction stir processing parameters on the mechanical properties of cast magnesium alloy AZ91. *Open Ind. Manuf. Eng.* **2010**, *2972*, 1–5. [CrossRef]
11. Cavaliere, P.; De Marco, P.P. Friction stir processing of AM60B magnesium alloy sheets. *Mater. Sci. Eng. A* **2007**, *462*, 393–397. [CrossRef]
12. Mishra, R.S.; Ma, Z.Y.; Charit, I. Friction Stir Processing: A novel technique for fabrication of surface composite. *Mater. Sci. Eng. A* **2003**, *341*, 307–310. [CrossRef]

13. Morisada, Y.; Fujii, H.; Nagaoka, T.; Fukusumi, M. Effect of friction stir processing with SiC particles on microstructure and hardness of AZ31. *Mater. Sci. Eng. A* **2006**, *433*, 50–54. [CrossRef]
14. Wang, W.; Shi, Q.Y.; Liu, P.; Li, H.K.; Li, T. A novel way to produce bulk SiCp reinforced aluminum Metal matrix composites by friction stir processing. *J. Mater. Process. Technol.* **2009**, *209*, 2099–2103. [CrossRef]
15. Sahraeinejad, S.; Izadi, H.; Haghshenas, M.; Gerlich, A.P. Fabrication of metal matrix composites by friction stir processing with different particles and processing parameters. *Mater. Sci. Eng. A* **2015**, *626*, 505–513. [CrossRef]
16. Shafiei-Zarghani, A.; Kashani-Bozorg, S.F.; Zarei-Hanzaki, A. Microstructures and mechanical properties of Al/Al_2O_3 surface nano-composite layer produced by friction stir processing. *Mater. Sci. Eng. A* **2009**, *500*, 84–91. [CrossRef]
17. Prakash, T.; Sivasankaran, S.; Sasikumar, P. Mechanical and tribological behaviour of friction-stir-processed Al 6061 aluminium sheet metal reinforced with Al_2O_3/0.5 Gr hybrid surface nanocomposite. *Arab. J. Sci. Eng.* **2014**, *40*, 559–569. [CrossRef]
18. Zakaria, H.M. Microstructural and corrosion behavior of Al/SiC metal matrix composites. *Ain Shams Eng. J.* **2014**, *5*, 831–838. [CrossRef]
19. Candan, S. Effect of SiC particle size on corrosion behavior of pressure infiltrated Al matrix composites in a NaCl solution. *Mater. Lett.* **2004**, *58*, 3601–3605. [CrossRef]
20. Abbass, M.K.; Hassan, K.S.; Alwan, A.S. Study of corrosion resistance of aluminum alloy 6061/SiC composites in 3.5% NaCl solution. *Int. J. Mater. Mech. Manuf.* **2015**, *3*, 31–35. [CrossRef]
21. Modi, O.P.; Saxena, M.; Prasad, B.K.; Jha, A.K.; Das, S.; Yegneswaran, A.H. Role of alloy matrix and dispersoid on corrosion behavior of cast aluminum alloy composites. *Corrosion* **1998**, *54*, 129–134. [CrossRef]
22. Feng, Z.; Lin, C.; Lin, J.; Luo, J.; Feng, Z.; Lin, C.; Lin, J. Pitting behavior of SiCp/2024 Al metal matrix composites. *J. Mater. Sci.* **1998**, *3*, 5637–5642. [CrossRef]
23. Sherif, E.M.; Almajid, A.A.; Latif, F.H.; Junaedi, H. Effects of graphite on the corrosion behavior of aluminum-graphite composite in sodium chloride solutions. *Corrosion* **2011**, *6*, 1085–1099.
24. Guo, M.L.T.; Tsao, C.-Y.A. Tribological behavior of self-lubricating aluminium/SiC/graphite hybrid composites synthesized by the semi-solid powder-densification method. *Compos. Sci. Technol.* **2000**, *60*, 65–74. [CrossRef]
25. Thapliyal, S.; Dwivedi, D.K. Microstructure evolution and tribological behavior of the solid lubricant based surface composite of cast nickel aluminum bronze developed by friction stir processing. *J. Mater. Process. Technol.* **2016**, *238*, 30–38. [CrossRef]
26. Liu, Y.; Rohatgi, P.K.; Ray, S. Tribological characteristics of aluminum-50 Vol Pct graphite composite. *Metall. Trans. A* **1993**, *24*, 151–159. [CrossRef]
27. Alaneme, K.K.; Sanusi, K.O. Microstructural characteristics, mechanical and wear behaviour of aluminium matrix hybrid composites reinforced with alumina, rice husk ash and graphite. *Eng. Sci. Technol. Int. J.* **2015**, *18*, 1–7. [CrossRef]
28. Saxena, M.; Modi, O.P.; Yegneswaran, A.H.; Rohatgi, P.K. Corrosion characteristics of cast aluminum alloy—3 wt % graphite particulate composites in different environments. *Corros. Sci.* **1987**, *27*, 249–256. [CrossRef]
29. Payan, S.; Le Petitcorps, Y.; Olive, J.-M.; Saadaoui, H. Experimental procedure to analyse the corrosion mechanisms at the carbon/aluminium interface in composite materials. *Compos. Part A Appl. Sci. Manuf.* **2001**, *32*, 585–589. [CrossRef]
30. Devaraju, A.; Kumar, A.; Kumaraswamy, A.; Kotiveerachari, B. Influence of reinforcements (SiC and Al_2O_3) and rotational speed on wear and mechanical properties of aluminum alloy 6061-T6 based surface hybrid composites produced via friction stir processing. *Mater. Des.* **2013**, *51*, 331–341. [CrossRef]
31. Aruri, D.; Adepu, K.; Adepu, K.; Bazavada, K. Wear and mechanical properties of 6061-T6 aluminum alloy surface hybrid composites [(SiC + Gr) and (SiC + Al_2O_3)] fabricated by friction stir processing. *J. Mater. Res. Technol.* **2013**, *2*, 362–369. [CrossRef]
32. Shahi, A.; Sohi, M.H.; Ahmadkhaniha, D.; Ghambari, M. In situ formation of Al-Al3Ni composites on commercially pure aluminium by friction stir processing. *Int. J. Adv. Manuf. Technol.* **2014**, *75*, 1331–1337. [CrossRef]
33. Elangovan, K.; Balasubramanian, V. Influences of pin profile and rotational speed of the tool on the formation of friction stir processing zone in AA2219 aluminium alloy. *Mater. Sci. Eng. A* **2007**, *459*, 7–18. [CrossRef]

34. Lee, W.B.; Yeon, Y.M.; Jung, S.B. Joint properties of friction stir welded AZ31B—H24 magnesium alloy. *Mater. Sci. Technol.* **2003**, *19*, 785–790. [CrossRef]
35. Armeyev, V.Y.; Chapliev, N.I.; Chistyakov, I.M.; Konov, V.I.; Ralchenko, V.G.; Strelnitsky, V.E.; Volkov, V.Y. Direct laser writing of microstructures in diamond-like carbon films. *Mater. Manuf. Process.* **1993**, *8*, 9–17. [CrossRef]
36. Sharma, A.; Sagar, S.; Mahto, R.P.; Sahoo, B.; Pal, S.K.; Paul, J. Surface modification of Al6061 by graphene impregnation through a powder metallurgy assisted friction surfacing. *Surf. Coat. Technol.* **2018**, *337*, 12–23. [CrossRef]
37. Sahoo, B.; Kumar, R.; Joseph, J.; Sharma, A.; Paul, J. Preparation of aluminium 6063-graphite surface composites by an electrical resistance heat assisted pressing technique. *Surf. Coat. Technol.* **2017**, *309*, 563–572. [CrossRef]
38. Sharma, A.; Sharma, V.M.; Mewar, S.; Pal, S.K.; Paul, J. Friction stir processing of Al6061- SiC -graphite hybrid surface composites. *Mater. Manuf. Process.* **2018**, *33*, 795–804. [CrossRef]
39. Tuinstra, F.; Koenig, L.; Koenig, J.L. Raman spectrum of graphite. *J. Chem. Phys.* **1970**, *53*, 1126–1130. [CrossRef]
40. Shi, Y.; Wang, D.; Zhang, J.; Zhang, P.; Shi, X.; Hao, Y. Synthesis of multilayer graphene films on copper by modified chemical vapor deposition. *Mater. Manuf. Process.* **2015**, *30*, 711–716. [CrossRef]
41. Sahoo, B.; Joseph, J.; Sharma, A.; Paul, J. Surface modification of aluminium by graphene impregnation. *Mater. Des.* **2017**, *116*, 51–64. [CrossRef]
42. Borriello, C.; De Maria, A.; Jovic, N.; Montone, A.; Schwarz, M.; Antisari, M.V. Mechanochemical exfoliation of graphite and its polyvinyl alcohol nanocomposites with enhanced barrier properties. *Mater. Manuf. Process.* **2009**, *24*, 1053–1057. [CrossRef]
43. Cullity, B.D.; Weymouth, J.W. Elements of X-ray diffraction. *Am. J. Phys.* **1957**, *25*, 394–395. [CrossRef]
44. Bartolucci, S.F.; Paras, J.; Rafiee, M.A.; Rafiee, J.; Lee, S.; Kapoor, D.; Koratkar, N. Graphene-aluminum nanocomposites. *Mater. Sci. Eng. A* **2011**, *528*, 7933–7937. [CrossRef]
45. Rhodes, C.G.; Mahoney, M.W.; Bingel, W.H.; Spurling, R.A.; Bampton, C.C. Effects of friction stir welding on microstructure of 7075 aluminum. *Scr. Mater.* **1997**, *36*, 69–75. [CrossRef]
46. Yadav, D.; Bauri, R. Nickel particle embedded aluminium matrix composite with high ductility. *Mater. Lett.* **2010**, *64*, 664–667. [CrossRef]
47. Amirkhanlou, S.; Jamaati, R.; Niroumand, B.; Toroghinejad, M.R. Manufacturing of high-performance Al356/SiC P composite by CAR process. *Mater. Manuf. Process.* **2011**, *26*, 902–907. [CrossRef]
48. Izadi, H.; Sandstrom, R.; Gerlich, A.P. Grain growth behavior and Hall–Petch strengthening in friction stir processed Al 5059. *Metall. Mater. Trans. A* **2014**, *45*, 5635–5644. [CrossRef]
49. Hihara, L.H.; Latanision, R.M. Galvanic corrosion of aluminum-matrix composites. *Corrosion* **1992**, *48*, 546–552. [CrossRef]
50. Sato, N. The stability of localized corrosion. *Corros. Sci.* **1995**, *37*, 1947–1967. [CrossRef]
51. Soib, M.; Selamat, B.I.N. Corrosion behavior of SiC P/6061 Al metal matrix composites in chloride solutions. *Adv. Perform. Mater.* **1996**, *3*, 183–204.
52. Abdi Behnagh, R.; Besharati Givi, M.K.K.; Akbari, M. Mechanical properties, corrosion resistance, and microstructural changes during friction stir processing of 5083 aluminum rolled plates. *Mater. Manuf. Process.* **2012**, *27*, 636–640. [CrossRef]
53. Zhang, F.; Huang, Y.; Hwang, K.C.; Qu, S.; Liu, C. A Three-dimensional strain gradient plasticity analysis of particle size effect in composite materials. *Mater. Manuf. Process.* **2007**, *22*, 140–148. [CrossRef]
54. Pardo, A.; Merino, M.C.; Rams, J.; Merino, S.; Viejo, F.; Campo, M. Effect of reinforcement coating on the oxidation behavior of AA6061/SiC/20p composite. *Oxid. Met.* **2005**, *63*, 215–227. [CrossRef]
55. Babu, J.; Srinivasan, A.; Kang, C. Nano and macromechanical properties of aluminium (A356) based hybrid composites reinforced with multiwall carbon nanotubes/alumina fiber. *J. Compos. Mater.* **2017**, *51*, 1631–1642. [CrossRef]